Magnetic Field Distributions of a Laser Assisted PulsedPlasma Thruster

IEPC-2015-475p／ISTS-2015-b-475p

Presented at Joint Conference of 30th International Symposium on Space Technology and Science
34th International Electric Propulsion Conference and 6th Nano-satellite Symposium,
Hyogo-Kobe, Japan
July 4 – 10, 2015

Kentaro Kato, Nao Akashi, Yuji Oigawa, Hiroshi Hosokawa, Hideyuki Horisawa
Department of Aeronautics and Astronautics, Tokai University, Hiratsuka, Kanagawa, 259-1292, Japan

To observe the plasma behaviors between the rectangular electrodes of the LA-PPT, an ICCD camera was utilized. From the time-resolved images, behaviors of the plasma wavefront were analyzed and speeds of the plasma were estimated. From the result, it was shown that regardless of the y-coordinates, the plasma wavefront was moving toward electrode edge. Larger speeds were obtained in anode side than cathode sides within the experimental conditions of this study. In addition faster motion of the wavefront of the plasma was observed in higher voltage cases. From the results, the typical speed of plasma for *V*c = 1000 V and 2000 V were 55 ± 2 km/s and 56 ± 2 km/s, respectively. Moreover, temporal variations of magnetic field distributions were measured by magnetic field probes located at various positions in the acceleration channel for *V*c = 1,000 V. From the result, the region of strong (or weak) plasma emission must be corresponding to the region of higher (or lower) discharge current density. Attached with the strong magnetic field region, the strong emission region is moving toward downstream. In addition, a stronger magnetic field can be only observed in the last quarter cycle in the first half cycle of the discharge current. From the temporal displacements of a wavefront of the strong magnetic field region, a speed of the wavefront was estimated as high as 59.8 km/s for *V*c = 1,000 V, which was in consistent with the results from ICCD images.

Nomenclature

B	=	magnetic field
d*t*	=	time step
N	=	winding number of magnetic field probe
V_c	=	capacitor voltage
I	=	ampere of discharge
Isp	=	specific impulse
h	=	electrode height
V_c	=	capacitor voltage

I. Introduction

The current trend towards small spacecraft, which is not only mass limited but also power limited, has produced a strong interest in development of micropropulsion devices.[1-4)] The significance in reducing launch masses has attracted growing interests in regard to a decrease in mission cost and an increase in launch rate. Although, in the past, many very small spacecraft lacked propulsion systems, future microspacecraft will require significant propulsion capability to provide a high degree of maneuverability and capability. The benefit of using electric propulsion for the reduction of spacecraft mass will likely be even more significant for mass limited micro- spacecraft missions.[2-4)] Feasibility studies of micro-spacecraft are currently under development for a mass less than 100 kg with an available power level for propulsion of less than 100 watts. [2-4)] Various potential propulsion systems for micro- spacecraft applications, such as ion thrusters, field emission thrusters, pulsed plasma thrusters (PPTs), vaporizing liquid thrusters, resistjets, microwave arcjets, pulsed arcjets, etc., have been proposed and are under significant development for primary and attitude control applications. [4] In particular, the PPTs are expected to be used for microsatellites and their long term missions because of the precise impulse bit controllability.

On the other hand, small-sized onboard laser plasma thrusters are also under significant development with rapid evolutions of novel compact laser systems. One of the advantages of the laser thrusters is that they can induce high specific impulses. In addition, the system can be very simple and small with significant controllability of the thrust. [5-8] To improve thrust performances and system simplicities of those conventional electric and laser propulsion systems, a preliminary study on a laser-electric hybrid acceleration system have been conducted by the authors.[9-15]

II. Laser assisted pulsed plasma thruster

A schematic of the rectangular laser-assisted pulsed plasma thruster (LA-PPT) is illustrated in Fig. 1.[9-15] A basic idea of the system is that a bunch of laser-ablation plasma, induced through laser irradiation on a solid target, is supplied to an acceleration channel and additionally accelerated by electrical means between an anode and a cathode. When the current between the electrodes increases, the plasma can be heated and further ionized through joule heating. Thus, the electrothermal acceleration effect will be significant. With larger current exceeding more than one thousand amperes, the electromagnetic acceleration effect becomes significant. With the interaction of the current and a self-induced magnetic field, a streamwise acceleration of the plasma will be provided.[17, 18]

Since any solid materials can be used for the propellant in these systems, no tanks, no valves, or piping systems are required for the propulsion system. Also, various materials in any phases can be used for the propellant. Therefore, the system employing this technique can be simple and compact. As the laser-ablation plasma has a directed initial velocity of tens of km/s, which will be further accelerated by electrical means, significantly high specific impulses can be expected.

III. . Research motivation

Figure 2 shows the typical high specific impulse characteristics of the laser-assisted pulsed plasma thruster replotted from our previous report, in which variations of specific impulse with charge energy are plotted for various acceleration channel configurations[15]. From the figure, it can be seen in all the cases that specific impulse increased with the increase of the charge energy. Moreover, thrusters with longer channel length showed higher specific impulses. The highest specific impulse of 7,200 sec was obtained with the 10 mm x 50 mm thruster at the highest charge energy of 8.6 J. However, the mechanism of generation of high specific impulses, or namely high speed plasmas, is still unknown.

Therefore, an objective of this study is to observe the plasma acceleration process and to estimate the speed of plasma from the results of image data. To observe the plasma behaviors between the rectangular electrodes of the LA-PPT, an ICCD camera was utilized. From the time-resolved images of the camera, behaviors of the plasma wavefront were analyzed and speeds of the plasma were estimated.

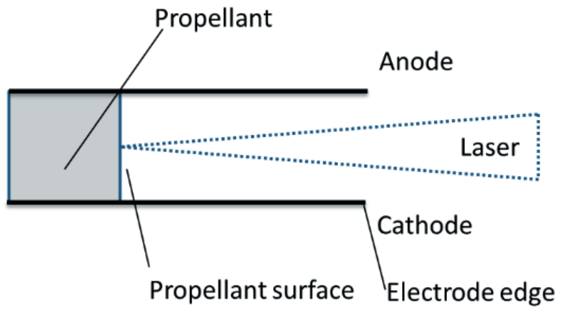

Figure2. Schematic of illustration of a rectangular laser-assisted pulsed plasma thruster (LA-PPT).

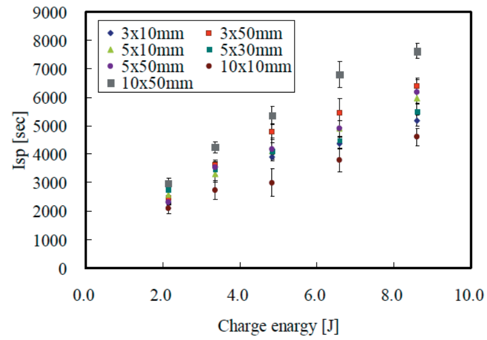

Figure1. Variation of specific impulse with charging energy for thrusters with various electrode geometries (electrode length × electrode height).[15]

IV. Experimental set up of Plasma behavior analysis

A. Plasma plume observation with ICCD camera

To observe the plasma behaviors between the rectangular electrodes of the LA-PPT, the time-resolved imaging with an ICCD camera was conducted. From the time-resolved images, behaviors of the plasma wave front were analyzed and speeds of the plasmas were estimated.

A photo of the thruster is shown in Fig. 3, in which electrodes made of molybdenum and propellant and insulator made of alumina ceramics. Configuration of the thruster is listedin Table 1. In this study, based on our previous results [16], relatively larger width and length of the rectangular electrodes of 10 mm x 50 mm were utilized, which showed the best thrust performance among various electrode configurations in our previous study.

A schematic of experimental set up for ICCD camera observation is shown in Fig. 4. The LA-PPT is placed in vacuum chamber (2.7×10^{-3} Pa) and ignited through a laser ablation plasma induced with a focused laser pulse at a center surface of the propellant. As for the laser oscillator, an Nd:YAG laser (CONTINUUM INC., Surelite II, wavelength: 1,064 nm, pulse width 5 ns, pulse energy: 400 mJ) was utilized. Time-resolved images were monitored with an ICCD camera (ANDOR TECHNOLOGY, minimum gate width: 2 ns).

Generating an arbitrary delay with a delay generator triggered by a Q-switch output signal of the laser, the ICCD camera was synchronized with single laser pulse and a discharge pulse, and then an image of the delay was captured at each pulse. Since the phenomena were highly reproducible, it was possible to obtain images of temporal behaviors of plasma formation and acceleration process with 2 ns resolution through changing the delay.

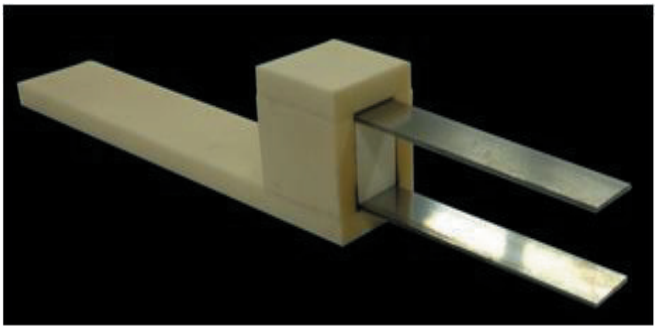

Figure3. Laser Assisted Pulsed Plasma Thruster (LA-PPT).

Table 1. Configuration of LA-PPT

Channel length: ***l***	50 mm
Channel width: ***w***	10 mm
Channel gap: ***h***	15 mm
Electrode material	Mo
Propellant material	Al_2O_3
Body	Al_2O_3

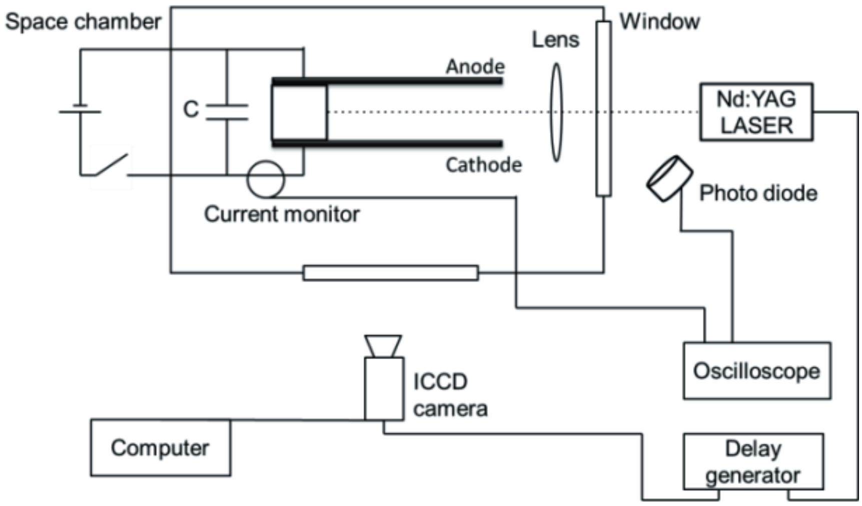

Figure4. Schematic of experimental set up for ICCD camera observation.

B. Plasma behavior analysis from ICCD images

Time-resolved images at different times were captured by the ICCD camera, and then analyzed with an image processing software. In the analysis, emission intensity distributions parallel to a longitudinal direction (*x*-axis) of the thruster were plotted and evaluated from the image data as shown schematically in Fig. 5. As shown in the figure, motion, or a velocity, of a wavefront (an inflection point of emission distribution) of plasma induced and accelerated in the thruster was extracted and evaluated. A typical interval (Δt) between two images was Δt = 100 ns for plasma velocity evaluation.

Since the plasma behaviors are non-uniform across the electrodes, plasma emission distributions and motions were evaluated along three lines (center line (y = 0 mm), anode side (y = 3 mm), cathode side (y = -3 mm)) parallel to a longitudinal axis (*x*-axis) of the thruster, as shown in Fig. 6.

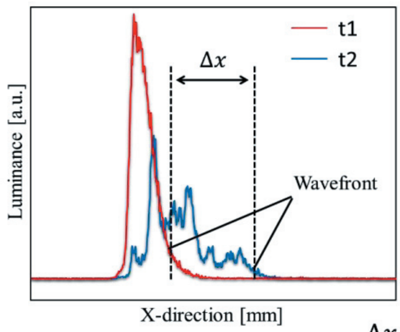

$$\Rightarrow v_p = \frac{\Delta x}{\Delta t}$$

Figure 5. Schematic of emission intensity distributions of the plasma parallel to x-axis of the thruster to determine motion of wavefront and velocity of plasma.

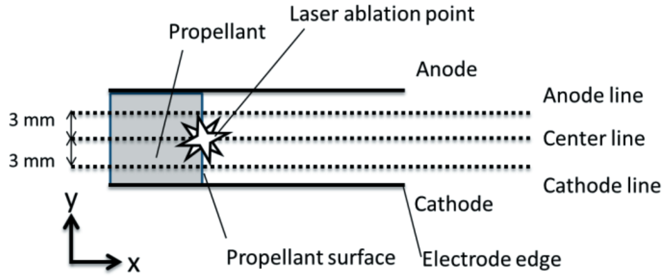

Figure6. Schematic illustration of three lines (center line(y=0 mm), cathode side (y = -3 mm), and anode side (y = 3 mm)) parallel to a longitudinal axis (x-axis) of the thruster.

C. Magnetic probe measurement

Temporal variations of magnetic field distributions in an acceleration channel, between anode and cathode, were estimated with magnetic probes. In this study, the magnetic probes were attached on a side wall (glass wall) of the acceleration channel, shown schematically in Fig.7, to insulate the coils from the electrodes. Each probe consists of a coil of a core diameter of 1 mm (3 turns of enameled copper wire of 0.6 mm in diameter). Positions of the magnetic probes on the glass wall, based on the rectangular coordinate system defined in Fig.6, are located at (x, y) = (0 mm, 7mm) for probe1, (x, y) = (0mm, 3.5mm) for probe2, (x, y) = (0 mm, 0mm) for probe3, (x, y) = (0 mm, -3.5mm) for probe4, and (x, y) = (0 mm, -7.5mm) for probe5, as shown in Fig.9. And, each probe can be moved to the electrode edge an x-axis stage.

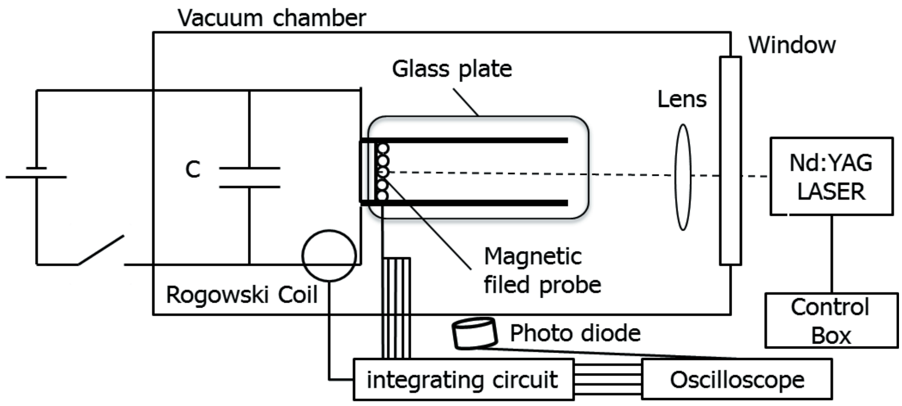

Figure 7.Schematic of experimental set up for magnetic field measurement.

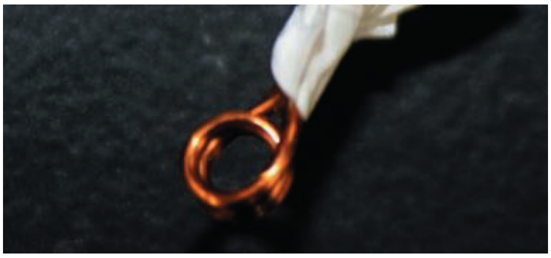

Figure8. Magnetic field probe

Table 2 Configuration of Magnetic field probe

Turns	3
Coil radius	
Material	Enameled Copper Wire

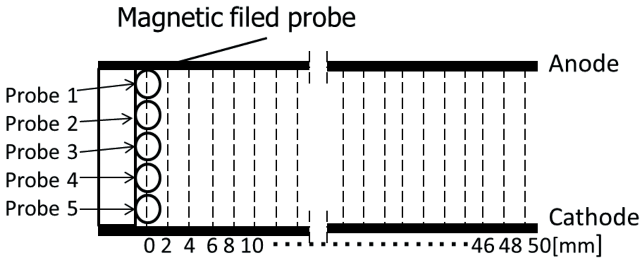

Figure9. Positions of magnetic probes on side wall of acceleration channel.

V. Results and Discussion

A. Plasma behavior observation with ICCD camera

ICCD images of plasma plume from a rectangular LA-PPT are shown in Fig. 10 for V_c = 1,000 V,. In these figures, white parts mean propellant surface and electrodes. The upper and lower electrodes are the anode and cathode, respectively.

For V_c= 1,000 V, in Fig.10, similar behaviors of the laser propulsion mode can be seen at 0 to 100 ns. However, at 200 ns, different from V_c = 0 V, a spot emission can be seen on the cathode surface. Therefore, the emission must be originated from discharge. At 400 ns, two planer emission structures can be seen, i.e., one near the cathode and another near the anode. At 400 ns, the anode side plasma is moving faster than that of cathode side. At 600 to 1,000 ns, a strong emission plume diffuses into *x*-direction after a sudden fall of intensity distribution at 600 ns. At 1000 ns, the plasma emission arrives at edges and strong emission can be seen at anode edge. On the other hand, after 1600 ns, the planer plasmas detach from the anode and extend to the cathode side. At 1,200 to 2,000 ns, a sudden fall of intensity distribution between electrodes and relatively stronger emission spots can be seen at the anode edge and cathode surface.

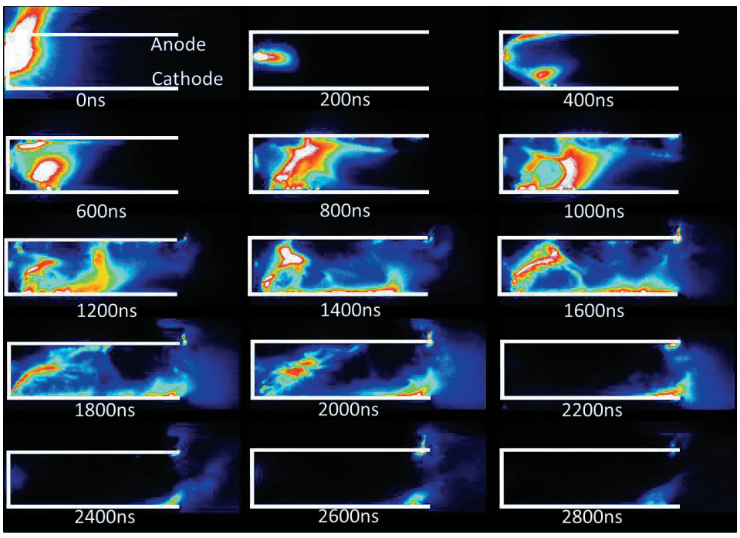

Figure 10. ICCD images of plume from a rectangular thruster (anode: higher electrode for td = 0-2800 ns,*Vc*=1kV)

B. Plasma behavior analysis

Time-resolved images captured by the ICCD camera were analyzed with image processing software. In the analysis, emission intensity distributions of the plasma parallel to a longitudinal direction (x-axis) of the thruster were plotted and evaluated from the image data, as shown in Fig. 11 (for y = 0 mm, V_c = 1,000 V, measured at 600 ns to 700 ns). From the figure, a wavefront was derived as an inflection point of each emission distribution. To determine the inflection point, the emission distribution data was smoothed with the moving averages of each 20-pixel data, and then derivatives were obtained. With this procedure, a deviation of the position of the wavefront was within 18 pixels, or namely within 2 mm before the edges of the thruster. In addition, a shot-to-shot deviation of the image was within ± 20 ns. Due to these errors, scatters of the speed of wavefront were within 5 %. From Fig. 11, a speed of the wavefront of the plasma in the thruster is v_p= 55 ± 2 km/s.

Temporal variations of the positions of wavefronts and local speeds of the wavefronts were plotted for V_c = 0 V, 1,000 V and 2,000 V in Fig. 12. From the figure, the maximum local speeds can be obtained at 100 ns, before which a laser ablation plasma was induced. After 100 ns, the speeds gradually decreased with time, and converged into above mentioned exhaust speeds. At 700 to 800 ns, the wavefronts reached at the edges of the electrodes. From the plasma speed of 56 ± 2 km/s at V_c = 2,000 V, a specific impulse estimated from the division of the speed by the gravitational acceleration (9.8 m/sec^2) gives I_{sp} = 5,700 sec. On the other hand, from our previous research, specific impulse data measured from the impulse and mass shot measurements shown in Fig. 3 gives I_{sp} ~ 7,200 sec[15]. This discrepancy of specific impulses estimated with the ICCD imaging is probably due to the presence of some invisible particles, i.e., fast ions, atoms, and neutral particles which are still invisible with conventional ICCD camera systems.

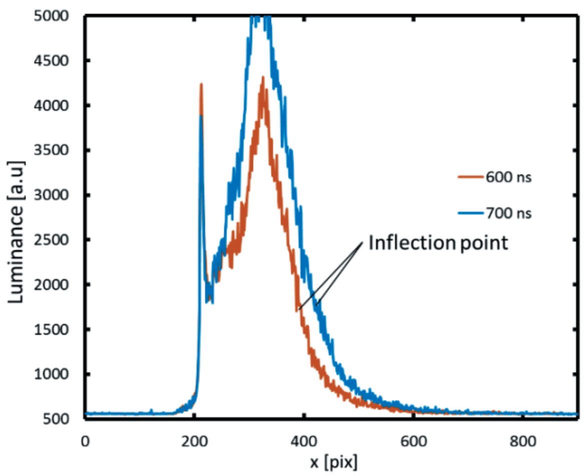

Figure11. Examples of emission intensity distributions of the plasma parallel to x-axis of the thruster to determine speed of plasma wavefront (for y = 0 mm, *Vc* =1,000 V. measured at 600 ns to 700 ns).

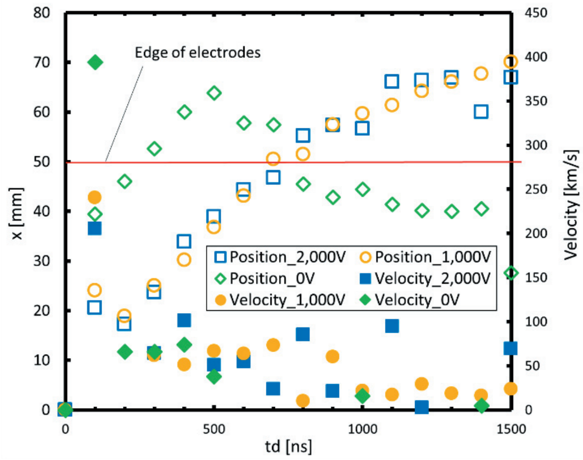

Figure12. Temporal variations of the positions of wavefronts and local speeds of the wavefronts were plotted for *Vc* = 0 V, 1,000 V and 2,000 V

C. Magnetic field measurement

Temporal variations of magnetic fields measured by the magnetic probes located at various positions are shown in Figs.13, 14 and 15 for V_c = 1,000 V. As can be seen, the magnetic fields in the acceleration channel were changing temporally and spatially. In general, it is presumed in PPT operation that the discharge current runs between electrodes forming a current sheet, and the motion of the current sheet is induced by an interaction of the discharge current in the current sheet and the self-induced magnetic field, or namely, Lorentz force. Associated with the motion of the current sheet, the motion of the magnetic fields in the acceleration channel will be induced. Since the magnetic probes are fixed on a side wall of the acceleration channel in this study, temporal variation of the magnetic field monitored with each probe includes positive and negative waveforms of the magnetic field. From the figures, it is shown that there are larger delays for the first positive (or negative) peaks at probes located at further downstream positions. These delays can be the durations for the magnetic field, or the current sheet, moving in the distances between the probes. Moreover, it can also be seen that temporal variations of the magnetic fields in regions at near propellant surface are almost in phase with a discharge current waveform. This implies that a portion of the discharge current is probably running at near surface of the propellant.

Temporal variations of the positions of magnetic field distributions were plotted for Vc = 1,000 V in Fig. 16. From the figure, at 900 ns, a strong magnetic field region can be observed at the propellant surface. At 1800 to 2000 ns, the strong magnetic field region reached at the edges of the electrodes. From the temporal displacements of a wavefront of the strong magnetic field region shown in Fig.16, a speed of the wavefront can be estimated as high as 59.8 km/s for Vc = 1,000 V, which is in consistent with the results from ICCD images.

From the results of Figs.13, 14 and 15, temporal variations of the magnetic field distribution in the acceleration channel are replotted in Fig.17 for *V*c = 1,000 V, in which corresponding ICCD images are also reviewed and compared. From the ICCD images, a canted plasma emission structure can be seen after 400 ns. At 800 ns, an anode side of the plasma is running faster than that of cathode side, and a strong emission region is extending toward an exhaust plane of the electrode edges. At 800 ns, in the magnetic field distribution, a strong positive magnetic field is induced in the near-surface region of the propellant, and then the strong magnetic field region is extending and moving toward the electrode edges from 1,200 to 2,000 ns. Comparing images of the magnetic field distribution and plasma emission distribution (ICCD images) at 800 ns, a strong magnetic field is induced in a left-side dark region of a strong plasma emission region, namely in the near-surface region of the propellant. At 1,200 ns, a strong magnetic field is induced in a dark region surrounded by electrodes and a plasma emission region. Similar tendencies can be seen at 1,400 to 1,800 ns.
From these results, the region of strong (or weak) plasma emission must be corresponding to the region of higher (or lower) discharge current density. Attached with the strong magnetic field region, the strong emission region is moving toward downstream.

Comparison of discharge current waveform and the images of the magnetic field and plasma emission in the acceleration channel are shown in Fig.18. From these figures, the strength of magnetic field at the time of D, in which the current has gone through the peak value and even falling, is stronger than the time of C, the time of peak current. At the time of E, showing the negative peak current, no regions with strong magnetic fields can be observed. Therefore, a stronger magnetic field can be only observed in the last quarter cycle in the first half cycle of the discharge current.

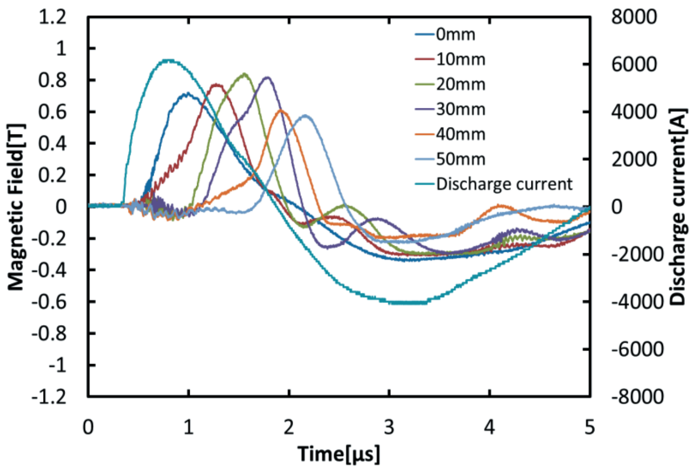

Figure13. Probe 1 signal at 0~50 mm from propellant surface (Vc =1,000V)

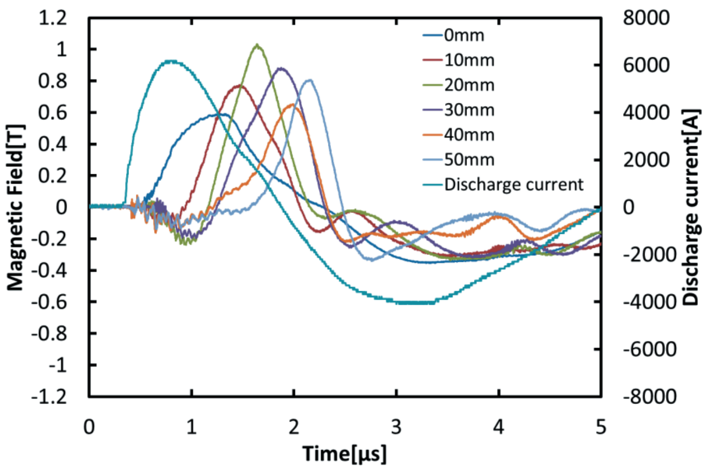

Figure14. Probe 3 signal at 0~50 mm from propellant surface (Vc =1,000V)

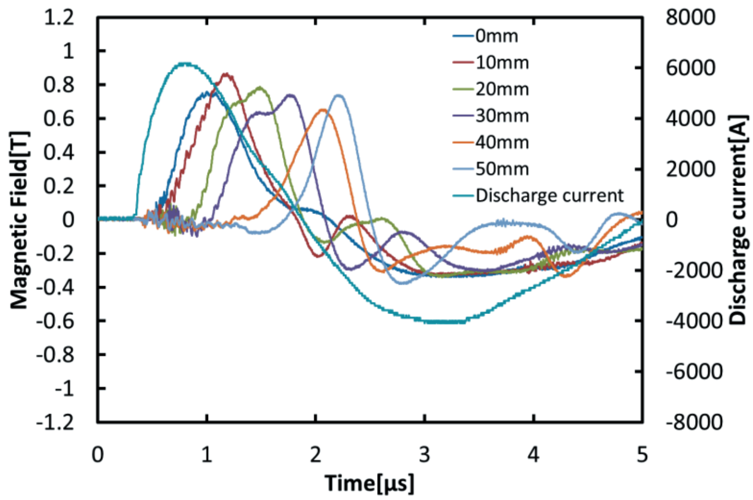

Figure15. Probe 5 signal at 0~50 mm from propellant surface (Vc =1,000V)

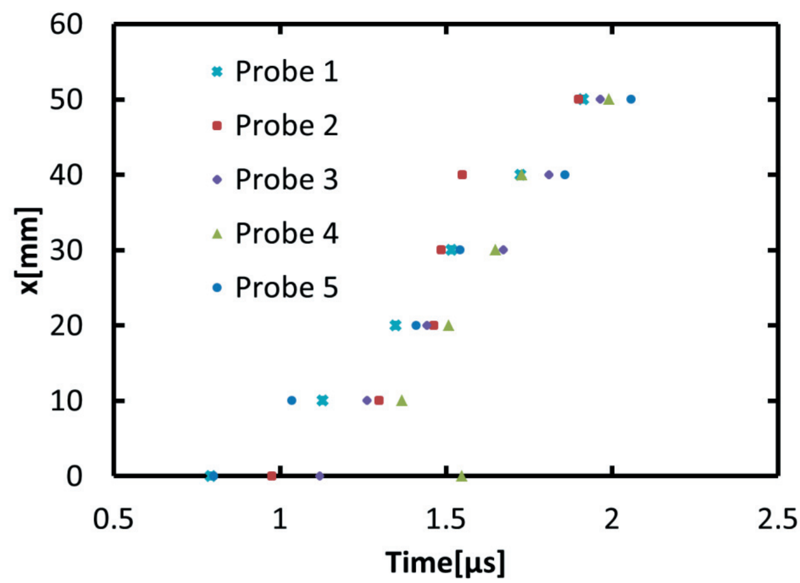

Figure 16. Temporal variations of the positions of magnetic field of positive peaks were plotted for Vc = 1,000 V.

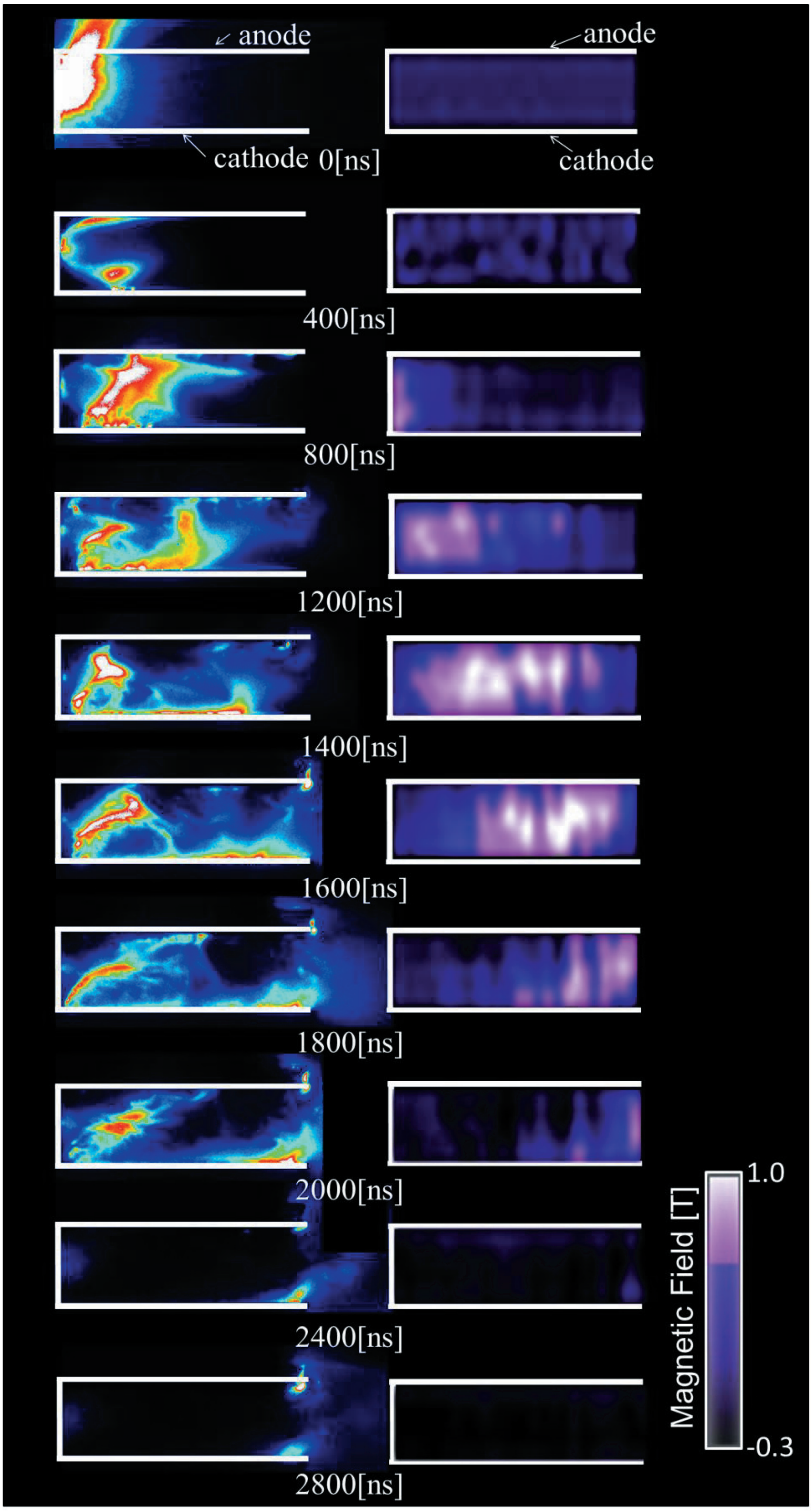

Figure.17 Temporal variation of magnetic field distribution (right) and ICCD camera images (left) in acceleration channel (for td = 0 ~ 2800 ns, Vc =1,000 V)

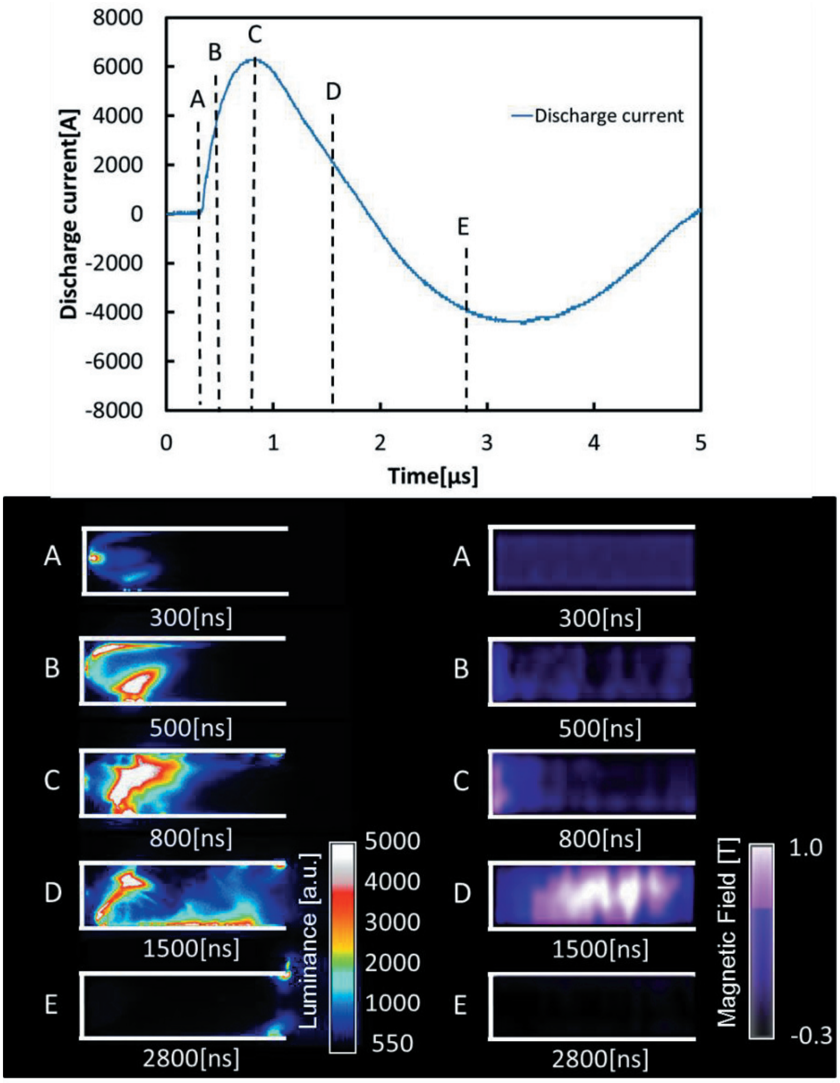

Figure.18 Comparison between discharge current waveform and magnetic field distribution (right) and ICCD images (left) for Vc = 1000 V.

VI. Conclusion

To observe the plasma behaviors between the rectangular electrodes of the LA-PPT, an ICCD camera was utilized. From the time-resolved images, behaviors of the plasma wavefront were analyzed and speeds of the plasma were estimated. From the result, it was shown that regardless of the y-coordinates, the plasma wavefront was moving toward electrode edge. Larger speeds were obtained in anode side than cathode sides within the experimental conditions of this study. In addition faster motion of the wavefront of the plasma was observed in higher voltage cases. From the results, the typical speed of plasma for Vc = 1000 V and 2000 V were 55 ± 2 km/s and 56 ± 2 km/s, respectively.

Moreover, temporal variations of magnetic field distributions were measured by magnetic field probes located at various positions in the acceleration channel for Vc = 1,000 V. From the result, the region of strong (or weak) plasma emission must be corresponding to the region of higher (or lower) discharge current density. Attached with the strong magnetic field region, the strong emission region is moving toward downstream. In addition, a stronger magnetic field can be only observed in the last quarter cycle in the first half cycle of the discharge current. From the temporal displacements of a wavefront of the strong magnetic field region, a speed of the wavefront was estimated as high as 59.8 km/s for Vc = 1,000 V, which was consistent with the results from ICCD images.

References

1) Myers, R. M., et al.: Small Satellite Propulsion Options, AIAA Paper, 1994, pp. 94-2997.

2) Mueller, J.: Thruster Options for Microspacecraft: A Review and Evaluation of Existing Hardware and Emerging Technologies, AIAA Paper, 1997, 97-3058,.

3) Leifer, S.: Overview of NASA's Advanced Propulsion Concepts Activities, AIAA Paper, 1998, 98-3183.

4) Micci, M. M., and Ketsdever, A. D. (ed.): Micropropulsion for Small Spacecraft, American Institute of Aeronautics and Astronautics, *Astronautics and Aeronautics.,* **187** (2000).

5) Gonzales, D., and Baker, R.: Micropropulsion Using a Nd:YAG Microchip Laser, Proceedings of SPIE

6) Pakhomov, A.V., et al.: Specific Impulse Study of Ablative Laser Propulsion, AIAA Paper, 2001, 2001-3663.

7) Horisawa, H., and Kimura I.: Fundamental Study on Laser Plasma Accelerator for Propulsion Applications, *Vacuum*, **65** (2002), pp.389-396.

8) Horisawa, H., et al., Beamed Energy Propulsion: AIP Conference Proceedings, **664** (2003), pp.423-432.

9) Kawakami, M., et al., AIAA Paper, 2003, 2003-5028.

10) Horisawa, H., et al., *Applied Physics A*., **81** (2005), pp.303-310.

11) Horisawa, H., et al., The Review of Laser Engineering., **34** (2006), pp.435-441.

12) Sasaki, Y., et al., IEPC (International Electric Propulsion Conference) Paper, 2007-56.

13) Horisawa, H., et al, AIAA Paper, 2008, 2008-4818.

14) Ono, T., et al, AIAA Paper, 2008, 2008-5008.

15) Horisawa, H.: High Isp Mechanism of Rectangular Laser-Electromagnetic Hybrid Acceleration Thruster, IEPC (International Electric Propulsion Conference) Paper IEPC-2011-274, pp. 7-8

16) T.E. Markusic.: Phenomenological Model of Current Sheet Canting in Pulsed Electromagnetic Accelerators, IEPC (International Electric Propulsion Conference) Paper, 2003, 2003-0293, pp. 5-6

17) Jahn, R. G.: *Physics of Electric Propulsion*, McGraw-Hill, 1968, pp.198-316.

18) Burton, R. L., and Turchi, P. J.: Pulsed Plasma Thruster, *Journal of Propulsion and Power.,* **14** (1998), pp. 716–735.

19) A. Nawaz, M. Lau, G. Herdrich, and M. Auweter-Kurtz. "Investigation of the Magnetic Field in a Pulsed Plasma Thruster", AIAA Journal, Vol. 46, No. 11 (2008), pp. 2881-2889.

20) T.E. Markusic, E.Y. Choueiri. "Photographic, magnetic, and interferometric measurements of current sheet canting in a pulsed electromagnetic accelerator" AIAA Paper, 2001 ,2001-3896